Full radiator-perturber interaction in computer simulations of hydrogenic spectral line broadening by plasmas

Evgeny Stambulchik [*]

Faculty of Physics, Weizmann Institute of Science, Rehovot 7610001, Israel

Carlos A. Iglesias [†]

Lawrence Livermore National Laboratories, P.O. Box 808, Livermore, California 94550, USA

Spectral line broadening by plasmas can be computed by solving the equation of motion for the dipole of the radiating system perturbed by a fluctuating potential obtained from computer simulations. Such calculations have relied on the multipole expansion of the radiator-plasma interaction often keeping only the dipole term. With increasing density, however, higher multipoles as well as plasma perturbers overlapping the bound electron wave functions are expected to become important. For hydrogenic systems, the atomic matrix elements of the full Coulomb and screened Coulomb interactions are given by analytical formulas. Using these results, a computer simulation approach that accounts for the full radiator-plasma interaction is developed. One benefit is the removal of inherent strong collision divergences in the multipole expansion approximation. Furthermore, it yields the plasma polarization shift produced by perturbers penetrating the wave function of the radiator bound electrons. The model was applied to hydrogenic argon Ly-α, Ly-β, and Ly-γ spectral lines in a dense argon plasma at free electron densities of 10^{24} or 10^{25} cm^{-3} and temperature of 800 eV relevant to plasma diagnostic techniques for inertial confinement fusion implosions.

I. INTRODUCTION

Computer simulations of spectral line broadening by plasmas have been performed for several decades [1–4]. Since the dipole interaction often dominates line broadening in plasmas [5], an essential ingredient for such calculations is time sequences of the fluctuating plasma electric field generated with molecular dynamics simulations. Given a field history, the Heisenberg equation of motion provides the time-dependent dipole of the radiating system used to compute the light amplitude correlation function.

In computer simulations for spectral line broadening the plasma perturbers move in classical trajectories. This semiclassical approach neglects quantum effects. For example, detailed balance is not satisfied for inelastic collisional excitation and deexcitation rates between atomic levels. This error is mitigated for plasma temperatures much larger than the energy level differences [3]. Nevertheless, even for degenerate systems detailed balance can impact line shift calculations [6]. Also neglected is exchange between perturbing and atomic electrons, which would tend to weaken the interaction between the plasma and the atomic system (henceforth the radiator) emitting or absorbing a photon.

Computer simulations of spectral line broadening have also assumed that on average the perturbers do not approach within the spatial radiator size. Hence, the radiator-perturber interaction is approximated by a multipole expansion typically retaining only the dipole interaction and in some cases the

quadrupole term [7,8]. This approximation was tested for electron collisions with highly charged ions in laser implosion experiments using full Coulomb radiator-perturber in perturbation theory [9]. The fortuitous overestimate of the dipole term simulating the full interaction occurred only at the lower densities and significant discrepancies were reported for denser plasmas. More recently the effect of penetrating collisions (perturbers significantly overlapping with bound electron wave functions) was considered for a large range of plasma densities in perturbation theory [10,11] and nonperturbative treatment [12] of electron impact broadening. Although the semiclassical and quantum mechanical treatments moderately disagree, both show significant differences with the dipole term in the multipole expansion at higher plasma densities. Finally, even though hydrogen spectral lines have been extensively studied, the subject is not closed. Unresolved inconsistencies have been reported in the Balmer series [13]. A possible issue is the assumed dipole only approximation for the radiator-plasma interaction [14,15].

Thus, extending the computer simulation approach by removing the multipole expansion approximation has been considered a priority development [16]. This is the goal of the present work. For nonrelativistic hydrogenic radiators the necessary matrix elements of the radiator-plasma interaction are analytic. Benefits of the full interaction are the removal of inherent strong collision divergences in multipole expansions and accounting for the monopole term [17] natively. A drawback is increased computational demands. Also discussed are similar formulations for the Debye screened radiator-perturber interaction often used to accelerate computer simulations by neglecting the mutual interaction between plasma particles.

[*]evgeny.stambulchik@weizmann.ac.il
[†]iglesias1@llnl.gov

The method is demonstrated for hydrogenic argon Ly-α, -β, and -γ spectral lines used to diagnose laser driven hot, dense plasmas relevant to inertial confinement experiments. Comparisons are made to calculations with a second-order perturbation treatment of the full-Coulomb interaction [9].

II. LINE SHAPE FUNCTION

The line shape function for a radiator emitting or absorbing a photon of energy $\hbar\omega$ is given by [5]

$$I(\omega) = \pi^{-1} \operatorname{Re} \int_0^\infty dt\, e^{i\omega t} \langle C(t) \rangle. \tag{1}$$

For dipole-allowed radiative transitions the correlation function of the light amplitude is

$$C(t) = \operatorname{Tr}[\rho \vec{d}(0) \cdot \vec{d}(t)], \tag{2}$$

where $\vec{d}$ and ρ are the dipole and density matrix for the radiator internal states, respectively, Tr denotes a trace over those states, and the brackets $\langle\ \rangle$ represent a statistical plasma average.

The line shape function here assumes independent Stark and Doppler broadening. Thus, it refers only to Stark broadening, and the operators are independent of the radiator center-of-mass variables. It is then convenient to place the origin of the coordinate system at the radiator nucleus. That is, the radiator is assumed to move at a constant velocity during the radiation process providing an inertial reference frame leading to the reduced mass model [18]. This approximation is convenient but not essential to computer simulations [19].

The time evolution of the radiator dipole operator is described by the Heisenberg equation

$$-i\hbar \frac{\partial}{\partial t} \vec{d}(t) = [H(t), \vec{d}(t)] \tag{3}$$

with $[\cdots, \cdots]$ a commutator and the time-dependent Hamiltonian

$$H(t) = H_0 + V_I(t), \tag{4}$$

where H_0 is the Hamiltonian for the unperturbed radiator and $V_I(t)$ is the time-dependent interaction produced by the perturbing plasma. Computer simulations provide the time-dependent interaction, and the resulting correlation function is averaged over time sequences [1].

The equation of motion represents a system of simultaneous equations for the matrix elements of the dipole operator. It is readily shown [20] that the matrix elements of the multipole expansion approximation for the radiator-plasma interaction can be expressed in terms of reduced matrix elements for electric multipole radiative transitions available from atomic packages [21,22]. Here analytical expressions are obtained for the full Coulomb and screened Coulomb interaction of nonrelativistic hydrogenic radiators.

III. COULOMB INTERACTION

The radiator-plasma interaction for a one-electron radiator is given by

$$V_{RP} = \sum_p Z_p \left(\frac{Z_N}{r_p} - \frac{1}{|\vec{r}_a - \vec{r}_p|} \right), \tag{5}$$

where the sum is over all plasma particles, Z_N is the radiator nuclear charge, $\vec{r}_a$ is the position of the bound electron, and $\vec{r}_p$ is the position of the pth perturber with electric charge Z_p. Atomic units are used henceforth with energy in hartree and length in Bohr radius.

The interaction can be separated as $V_{RP} = V_{\text{net}} + V_I$, where the first term represents the plasma interacting with the net radiator point charge located at the origin,

$$V_{\text{net}} = (Z_N - 1) \sum_p \frac{Z_p}{r_p}. \tag{6}$$

The second term is the interaction of the plasma with the radiator internal states

$$V_I = \sum_p Z_p u(\vec{r}_a, \vec{r}_p) \tag{7}$$

with

$$
\begin{aligned}
u(\vec{r}_a, \vec{r}) &= \frac{1}{r} - \frac{1}{|\vec{r}_a - \vec{r}|} \\
&= \sum_{\ell m} \frac{4\pi}{2\ell + 1} \left(\frac{\delta_{\ell 0}}{r} - \frac{r_<^\ell}{r_>^{\ell+1}} \right) Y_{\ell m}^*(\hat{r}) Y_{\ell m}(\hat{r}_a),
\end{aligned} \tag{8}
$$

where $r_<$ ($r_>$) is the smaller (larger) of $r_a = |\vec{r}_a|$ and $r_p = |\vec{r}_p|$, $Y_{\ell m}(\hat{x})$ is a spherical harmonic with $\hat{x}$ a unit vector in the direction of $\vec{x}$, and the superscript $*$ denotes complex conjugate. The potential V_{net} is typically grouped with the Hamiltonian for the plasma since it is independent of the radiator internal states. Thus, it commutes with the radiator dipole and does not explicitly appear in the dipole equation of motion in Eq. (3). For charged radiators, however, it does affect the relative motion of the perturbers about the radiator.

A. Multipole expansion

The multipole expansion always assumes $r > r_a$ and the matrix elements simplify to

$$\langle \alpha | V_I | \beta \rangle \xrightarrow[r > r_a]{} (-1)^{J_\alpha - M_\alpha} \sum_{\ell \geqslant 1} \sum_m \begin{pmatrix} J_\alpha & \ell & J_\beta \\ -M_\alpha & m & M_\beta \end{pmatrix} q_{\alpha\beta}^{(\ell)} \Phi_{\ell m}^* \tag{9}$$

that factors into separate radiator and plasma contributions with J and M the total and magnetic quantum numbers of the internal radiator state, respectively. Note that the $\ell = 0$ term is absent in the multipole expansion approximation since the net radiator charge is treated through V_{net}. The plasma-dependent factor is given by

$$\Phi_{\ell m}^* = -\sqrt{\frac{4\pi}{2\ell + 1}} \sum_p \frac{Z_p}{r_p^{\ell+1}} Y_{\ell m}^*(\hat{r}_p) \tag{10}$$

and conforms with usual electrodynamics convention (e.g., electric field lines flow away from positive charges). Note that

$$\Phi_{\ell, -m}^* = (-1)^m \Phi_{\ell m}. \tag{11}$$

Therefore, there are $2\ell + 1$ independent real quantities for each multipole: ℓ complex numbers for the $m > 0$ terms plus one real number for the $m = 0$ term. For example, the three components of the plasma electric field, five elements of the symmetric traceless $\vec{\nabla} \vec{F}$ tensor (the total plasma electric field

$\vec{F}$ at the origin satisfies the Laplace equation), and so on for higher multipoles.

The radiator moments are independent of plasma variables and given in terms of atomic reduced matrix elements of the Wigner-Eckart theorem [21],

$$
\begin{aligned}
q_{\alpha\beta}^{(\ell)} &= \sqrt{\frac{4\pi}{2\ell+1}} \langle \Gamma_\alpha J_\alpha \| r_a^\ell Y_{\ell m}(\hat{r}_a) \| \Gamma_\beta J_\beta \rangle \\
&= A_{\alpha\beta}^{(\ell)} R_{\alpha\beta}^{(\ell)}
\end{aligned}
\tag{12}
$$

with Γ the remaining quantum numbers to identify the internal radiator state $|\Gamma J M\rangle$. The angular integration results are in $A_{\alpha\beta}^{(\ell)}$ and the radial integrals are given by

$$
R_{\alpha\beta}^{(\ell)} = \int_0^\infty dr_a P_\alpha(r_a) r_a^\ell P_\beta(r_a)
\tag{13}
$$

with $P_\alpha(r)$ the reduced radial wave function for radiator internal state $|\alpha\rangle$. The reduced matrix elements in Eq. (12) are the same as those for electric multipole radiative transitions [21]. For hydrogenic radiators, the angular contribution is given in Appendix A, and the radial integrals yield analytical results provided in Appendix B for cases used in the present work.

B. Full Coulomb interaction

In contrast to the multipole expansion approximation, the full Coulomb radiator-plasma interaction includes penetration of the radiator by a plasma perturber. In this case, the matrix elements no longer factor into independent radiator and plasma contributions,

$$
\langle \alpha | V_I | \beta \rangle = (-1)^{J_\alpha - M_\alpha} \sum_{\ell m} \begin{pmatrix} J_\alpha & \ell & J_\beta \\ -M_\alpha & m & M_\beta \end{pmatrix} A_{\alpha\beta}^{(\ell)} \Xi_{\alpha\beta;\ell m}^*,
\tag{14}
$$

where

$$
\Xi_{\alpha\beta;\ell m}^* = \sum_p Z_p U_{\alpha\beta}^{(\ell)}(r_p) \sqrt{\frac{4\pi}{2\ell+1}} Y_{\ell m}^*(\hat{r}_p)
\tag{15}
$$

also satisfying a relation like Eq. (11). For the reduced matrix elements (see Appendix A)

$$
\sqrt{\frac{4\pi}{2\ell+1}} \langle \Gamma_\alpha J_\alpha \| \left(\frac{\delta_{\ell 0}}{r} - \frac{r_<^\ell}{r_>^{\ell+1}} \right) Y_{\ell m}(\hat{r}_a) \| \Gamma_\beta J_\beta \rangle = A_{\alpha\beta}^{(\ell)} U_{\alpha\beta}^{(\ell)}(r)
\tag{16}
$$

with radial matrix elements

$$
U_{\alpha\beta}^{(\ell)}(r) = \int_0^\infty dr_a P_\alpha(r_a) \left(\frac{\delta_{\ell 0}}{r} - \frac{r_<^\ell}{r_>^{\ell+1}} \right) P_\beta(r_a).
\tag{17}
$$

Contrary to the long-ranged multipole expansion with radiator moments $q_{\alpha\beta}^{(\ell)}$, the radiator radial matrix elements $U_{\alpha\beta}^{(\ell)}(r)$ depend on the perturber radial positions. For hydrogenic systems the matrix elements have analytical results [23], and examples are given in Appendix B.

It is possible to rewrite Eq. (17) for $\ell \geq 1$ as

$$
U_{\alpha\beta}^{(\ell)}(r) = -\frac{R_{\alpha\beta}^{(\ell)}}{r^{\ell+1}} \left[1 - e^{-(n_a+n_b)Z_N r/(n_a n_b)} p_{\alpha\beta}^{(\ell)}(r) \right],
\tag{18}
$$

where $p_{\alpha\beta}^{(\ell)}(r)$ is a polynomial in r. The first term represents the long-ranged contribution of the ℓ multipole. The second
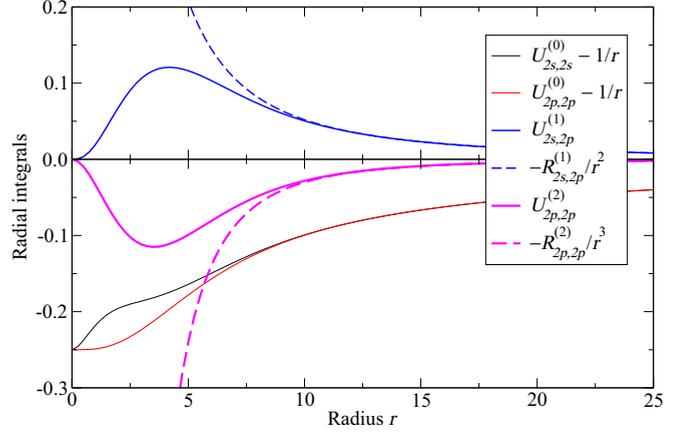

FIG. 1. Plots of the radial integrals $U_{\alpha\beta}^{(\ell)}(r)$ and their multipole equivalents $-R_{\alpha\beta}^{(\ell)}/r^{\ell+1}(r)$ for the $n=2$ levels in hydrogen. The divergent $1/r$ term subtracted from the $\ell=0$ integrals. Axes labeled in the atomic units.

term accounts for penetrating collisions, which vanish exponentially with the perturber radial position. This suggests that the sum over perturbers in Eq. (15) can be separated into near and far perturbers. That is, only the long-ranged multipoles are needed for perturbers far from the radiator.

C. Strong collisions for $\ell \geq 1$

As shown previously for $\ell \geq 1$ [9–11,24], the radiator-plasma interaction is softened by penetrating collisions relative to the multipole expansion approximation. The monopole term, however, requires special attention and is discussed in Sec. III D.

The radial matrix elements for $\ell \geq 1$ are given by

$$
\begin{aligned}
U_{\alpha\beta}^{(\ell \geq 1)}(r) = &-\frac{1}{r^{\ell+1}} \int_0^r dr_a P_\alpha(r_a) r_a^\ell P_\beta(r_a) \\
&- r^\ell \int_r^\infty \frac{dr_a}{r_a^{\ell+1}} P_\alpha(r_a) P_\beta(r_a)
\end{aligned}
\tag{19}
$$

and, therefore, $\propto r^\ell$ for $r \to 0$ except for special cases when the second integral vanishes [25]. Using $P_\mu(x \to 0) \propto x^{\ell_\mu+1}$ [26] and the triangle inequality $|\ell_\alpha - \ell_\beta| \leq \ell \leq \ell_\alpha + \ell_\beta$ [imposed by the $3j$ symbol in Eq. (A2)],

$$
U_{\alpha\beta}^{(\ell \geq 1)}(r \to 0) \propto \begin{cases} r^{\ell_\alpha+\ell_\beta+2}, & n_\alpha = n_\beta, \ell = |\ell_\alpha - \ell_\beta| \\ r^\ell, & \text{otherwise} \end{cases}
\tag{20}
$$

and vanish with decreasing radial distance. Consequently, the full Coulomb interaction eliminates divergences from strong collisions for $\ell \geq 1$ in the long-ranged multipole expansions. Plots of the radial integrals for $n=2$ of hydrogen are presented in Fig. 1. The figure shows the multipole expansion in agreement with the full Coulomb results at larger distances but diverging at small radii. It also shows the full Coulomb interaction softening the multipole expansion approximation avoiding the divergence at small radii. Note that the radial matrix elements from $\ell=1$ and $\ell=2$ are comparable in magnitude except the latter decays faster with radial separation.

D. Strong collisions for monopole

The $\ell = 0$ matrix elements of V_I are diagonal in orbital angular momentum (see Appendix A) and for hydrogenic radiators can differ only in principal quantum number. Thus, Eq. (17) yields

$$
\begin{aligned}
U^{(0)}_{n_\alpha \ell_\alpha, n_\beta \ell_\beta}&(r \to 0) \\
&= \delta_{n_\alpha n_\beta}\left(\frac{1}{r} - \frac{Z_N}{n_\alpha^2}\right) - (1 - \delta_{n_\alpha n_\beta}) \\
&\quad \times \int_0^\infty \frac{dr_a}{r_a} P_{n_\alpha \ell_\alpha}(r_a) P_{n_\beta \ell_\alpha}(r_a) + O(r^{2\ell_\alpha + 2})
\end{aligned}
\tag{21}
$$

and the diagonal matrix elements diverge at the origin; a consequence of the $1/r$ term in Eq. (8).

To proceed, consider the coupled equations of motion in matrix notation,

$$
\begin{aligned}
-i\frac{\partial}{\partial t}\vec{d}_{\alpha\beta} &= \langle \alpha | [H_0, \vec{d}] | \beta \rangle \\
&\quad + \sum_\mu (\langle \alpha | V_I | \mu \rangle \vec{d}_{\mu\beta} - \vec{d}_{\alpha\mu}\langle \mu | V_I | \beta \rangle).
\end{aligned}
\tag{22}
$$

When a perturber is very close to the radiator nucleus at radial position r_{NN} with charge Z_{NN}, the interaction is dominated by the divergent term in Eq. (21). Thus, Eq. (22) can be written as

$$
\begin{aligned}
-i\frac{\partial}{\partial t}\vec{d}_{\alpha\beta} &= \langle \alpha | [H_0 + V_I', \vec{d}] | \beta \rangle \\
&\quad + Z_{NN}\sum_\mu \left(\langle \alpha | r_{NN}^{-1} | \mu \rangle \vec{d}_{\mu\beta} - \vec{d}_{\alpha\mu}\langle \mu | r_{NN}^{-1} | \beta \rangle\right) \\
&= \langle \alpha | [H_0 + V_I', \vec{d}] | \beta \rangle
\end{aligned}
\tag{23}
$$

using the orthogonality condition $\langle \alpha | \beta \rangle = \delta_{\alpha\beta}$ with V_I' the remaining contributions to the interaction. Thus, the divergent terms from close collisions cancel in the time development of the radiator dipole. Note that the no-lower-state broadening approximation common in many calculations cannot be applied to the monopole term in the full Coulomb radiator-perturber interaction and avoid the divergence in Eq. (21). Although the discussion about divergences was applied to the equation of motion for dipole allowed transitions in Eq. (2), the cancellation of the divergence is general and applies to any transition.

IV. SCREENED COULOMB INTERACTION

In trivial molecular dynamics (TMD) simulations, the mutual interaction between plasma particles is neglected significantly accelerating the computer simulations [27]. To mimic plasma effects, a Debye screened radiator-perturber interaction is introduced. Thus,

$$
V_{RP} \to V^s_{RP} = \sum_\sigma Z_\sigma \sum_{p \in \sigma}\left(\frac{Z_N e^{-\kappa_\sigma r}}{r_p} - \frac{e^{-\kappa_\sigma |\vec{r}_a - \vec{r}_p|}}{|\vec{r}_a - \vec{r}_p|}\right).
\tag{24}
$$

This expression accounts for different inverse screening Debye lengths κ_σ for different plasma species σ with charge Z_σ.

A. Partial wave expansion

The separation of the interaction has $V^s_{RP} = V^s_{\text{net}} + V^s_I$ where

$$
V^s_{\text{net}} = (Z_N - 1)\sum_\sigma Z_\sigma \sum_{p \in \sigma}\frac{e^{-\kappa_\sigma r}}{r_p}
\tag{25}
$$

and

$$
V^s_I = \sum_\sigma \sum_{p \in \sigma} Z_p u(\vec{r}_a, \vec{r}_p; \kappa_\sigma)
\tag{26}
$$

with

$$
\begin{aligned}
u(\vec{r}_a, \vec{r}; \kappa) &= \frac{e^{-\kappa r}}{r} - \frac{e^{-\kappa|\vec{r}_a - \vec{r}|}}{|\vec{r}_a - \vec{r}|} \\
&= \sum_{\ell m}\left[\delta_{\ell 0}\frac{e^{-\kappa r}}{r} - \frac{4\pi}{\sqrt{r_a r}}I_{\ell + \frac{1}{2}}(\kappa r_<) \right. \\
&\quad \left. \times K_{\ell + \frac{1}{2}}(\kappa r_>)Y^*_{\ell m}(\hat{r})Y_{\ell m}(\hat{r}_a)\right].
\end{aligned}
\tag{27}
$$

Here I and K are modified Bessel functions of the first and third kind [26]. It is emphasized that the partial wave expansion is exact and contrary to previous work [7,8,28,29] that assumed $\kappa r_a \ll 1$ does not neglect radiator size effects [20,30].

The full screened Coulomb radiator-plasma interaction includes penetration of the radiator by a plasma perturber, and as in the unscreened case, the matrix elements do not factor into independent radiator and plasma contributions,

$$
\langle \alpha | V^s_I | \beta \rangle = (-1)^{J_\alpha - M_\alpha}\sum_{\ell m}\begin{pmatrix} J_\alpha & \ell & J_\beta \\ -M_\alpha & m & M_\beta \end{pmatrix}A^{(\ell)}_{\alpha\beta}\Xi^{s*}_{\alpha\beta;\ell m},
\tag{28}
$$

where

$$
\Xi^{s*}_{\alpha\beta;\ell m} = \sum_\sigma Z_\sigma \sum_{p \in \sigma} U^{(\ell)}_{\alpha\beta}(r_p; \kappa_\sigma)\sqrt{\frac{4\pi}{2\ell + 1}}Y^*_{\ell m}(\hat{r}_p),
\tag{29}
$$

which also satisfy a relation like Eq. (11). The radial matrix elements are defined by

$$
\begin{aligned}
U^{(\ell)}_{\alpha\beta}(r; \kappa) &= \delta_{\alpha\beta}\delta_{\ell 0}\frac{e^{-\kappa r}}{r} - \frac{2\ell + 1}{\sqrt{r}}\int_0^\infty \frac{dr_a}{\sqrt{r_a}} \\
&\quad \times P_\alpha(r_a)I_{\ell + \frac{1}{2}}(\kappa r_<)K_{\ell + \frac{1}{2}}(\kappa r_>)P_\beta(r_a).
\end{aligned}
\tag{30}
$$

Using expansions for the modified Bessel functions [26], it is readily shown that

$$
U^{(\ell)}_{\alpha\beta}(r; \kappa \to 0) = U^{(\ell)}_{\alpha\beta}(r),
\tag{31}
$$

reproducing the Coulomb interaction result. The integrals in Eq. (30) converge for $\kappa \geqslant 0$ and for nonrelativistic hydrogenic systems yield analytic results. The results, however, are more complicated than for the Coulomb interaction in Sec. III.

B. Separation of multipole expansion

For expediency in trivial computer simulations following the discussion after Eq. (18), the long-ranged multipole contribution is explicitly separated,

$$
U^{(\ell)}_{\alpha\beta}(r; \kappa) = R^{(\ell)}_{\alpha\beta}(\kappa)G_\ell(r; \kappa) + B^{(\ell)}_{\alpha\beta}(r; \kappa),
\tag{32}
$$

valid for $\ell \geqslant 0$. The κ-dependent radiator radial moments are given by

$$R_{\alpha\beta}^{(\ell)}(\kappa) = -\delta_{\alpha\beta}\delta_{\ell 0} + \frac{(2\ell+1)!!}{\kappa^{\ell}}$$
$$\times \int_0^{\infty} dr_a P_{\alpha}(r_a)\sqrt{\frac{\pi}{2\kappa r_a}}I_{\ell+\frac{1}{2}}(\kappa r_a)P_{\beta}(r_a) \quad (33)$$

and plasma fields

$$G_{\ell}(r;\kappa) = -\frac{\kappa^{\ell+1}}{(2\ell-1)!!}\sqrt{\frac{2}{\pi\kappa r}}K_{\ell+\frac{1}{2}}(\kappa r), \quad (34)$$

where $(-1)!! = 1$. These definitions are chosen so that the no screening limit, obtained by expanding the Bessel functions to lowest nonvanishing order, yields

$$R_{\alpha\beta}^{(\ell)}(\kappa \to 0) = \begin{cases} \frac{\kappa^2}{6}R_{\alpha\beta}^{(2)} + O(\kappa^4), & \ell = 0 \\ R_{\alpha\beta}^{(\ell)} + O(\kappa^2), & \ell \geqslant 1 \end{cases} \quad (35)$$

and

$$G_{\ell}(r;\kappa \to 0) = -\frac{1}{r^{\ell+1}}, \quad (36)$$

reproducing the Coulomb results. As discussed in [30], the $\ell = 0$ term does not vanish in the long-ranged multipole expansion of the screened Coulomb radiator-perturber interaction due to the radiator finite size and the cloud associated with the screening of each plasma particle.

The short-ranged contributions are defined by

$$B_{\alpha\beta}^{(\ell)}(r;\kappa) = (2\ell+1)\int_r^{\infty}\frac{dr_a}{\sqrt{r_a r}}P_{\alpha}(r_a)P_{\beta}(r_a)$$
$$\times \left[I_{\ell+\frac{1}{2}}(\kappa r_a)K_{\ell+\frac{1}{2}}(\kappa r) - I_{\ell+\frac{1}{2}}(\kappa r)K_{\ell+\frac{1}{2}}(\kappa r_a)\right]. \quad (37)$$

Note that the separation in Eq. (32) requires

$$\kappa < Z_N \frac{n_{\alpha}+n_{\beta}}{n_{\alpha}n_{\beta}} \quad (38)$$

to avoid divergences. This constrain is satisfied except for extreme plasma conditions when the screening length is smaller than the atomic state effective size. For nonrelativistic hydrogenic systems the radial integrals yield analytic results, and examples are provided in Appendix C.

C. Weak collisions

The contributions from penetrating collisions in Eq. (37) decay exponentially with the perturber distance to the radiator nucleus (see Appendix D),

$$B_{\alpha\beta}^{(\ell)}(r;\kappa) \propto e^{-(n_{\alpha}+n_{\beta})r/(n_{\alpha}n_{\beta})}. \quad (39)$$

Consequently, for distant perturbers it is possible to neglect $B_{\alpha\beta}^{(\ell)}(r;\kappa)$ and only retain the multipole expansion term in Eq. (32),

$$M_{\alpha\beta}^{(\ell)}(r;\kappa) = R_{\alpha\beta}^{(\ell)}(\kappa)G_{\ell}(r;\kappa). \quad (40)$$

In the Coulomb interaction limit, the expression reduces to

$$M_{\alpha\beta}^{(\ell)}(r;\kappa=0) = -\frac{R_{\alpha\beta}^{(\ell)}}{r^{\ell+1}}, \quad \ell \geqslant 1, \quad (41)$$

and the sum over partial waves ℓ converges rapidly for sufficiently large radii.

For the screened Coulomb interaction, the large radii limit of Eq. (40) is given by

$$M_{\alpha\beta}^{(\ell)}(r \to \infty;\kappa) = \frac{e^{-\kappa r}}{r}\left[\delta_{\ell 0} - (2\ell+1)\int_0^{\infty}dr_a\right.$$
$$\left.\times P_{\alpha}(r_a)\sqrt{\frac{\pi}{2\kappa r_a}}I_{\ell+\frac{1}{2}}(\kappa r_a)P_{\beta}(r_a)\right], \quad (42)$$

and the partial waves do not display the $r^{-(\ell+1)}$ behavior in the pure Coulomb case. Typically, the plasma conditions are such that the effective radiator size is much smaller than the plasma screening length and expanding the Bessel function leads to a power series,

$$\sum_{\ell=0} M_{\alpha\beta}^{(\ell)}(r \to \infty;\kappa)$$
$$\xrightarrow[\kappa r_a \ll 1]{} \frac{e^{-\kappa r}}{r}\sum_{j=1}^{\infty}c_j\int_0^{\infty}dr_a P_{\alpha}(r_a)(\kappa r_a)^j P_{\beta}(r_a) \quad (43)$$

with c_j an expansion constant and the sum over j (not the same as partial waves ℓ) converges since effectively $\kappa r_a \ll 1$. For example, for $n = 2$ levels of a hydrogenic ion (see Appendix C)

$$\lim_{r \to \infty}\frac{M_{2p,2p}^{(2)}(r;\kappa)}{M_{2s,2p}^{(1)}(r;\kappa)} = \frac{10Z_N^2}{3\sqrt{3}(Z_N^2+\kappa^2)}\left[Z_N\kappa - \frac{2}{Z_N r} + O(r^{-2})\right]. \quad (44)$$

This ratio goes as r^{-1} for $\kappa \to 0$, and the interaction approaches the pure Coulomb potential but goes to $\sim 0.962 Z_N^2$ as κ approaches the maximum value Z_N [see Eq. (38)]. The present work (see Sec. V) is consistent to order $\kappa^2 r_a^2$ [11] retaining up to the quadrupole term in the multipole expansion.

D. Strong collisions

The screening of the radiator-plasma interaction has negligible effect on close collisions. As such, the small r dependence of the radial integrals for the screened Coulomb radiator-plasma interaction follows closely those for the unscreened results again leading to vanishing terms for $\ell \geqslant 1$ and canceling divergences for the monopole term.

E. Comparison of monopole terms

The radial integrals for the monopole terms are presented in Fig. 2 for the $1s$ level of neutral hydrogen with $\kappa = 0.1$ for the screened matrix elements. In addition, the figure displays the screening function

$$S(r) = 1 - \int_0^r dr_a[P_{1s}(r_a)]^2$$
$$= e^{-2r}(1 + 2r + 2r^2), \quad (45)$$

which represents the screening of the nucleus by the bound electron. As shown in Fig. 2, the $\ell = 0$ matrix element for the Coulomb interaction vanishes outside the effective size of the radiator because the bound electron fully screens the nucleus. There is, however, a significant different behavior
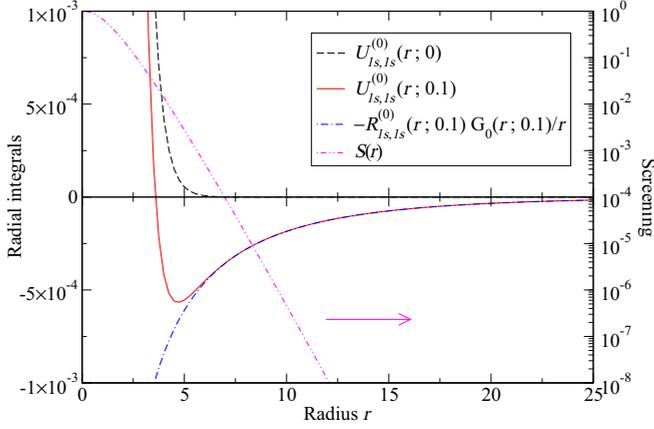
FIG. 2. Plots of the radial integrals $U_{1s,1s}^{(0)}(r;\kappa)$ and $-R_{1s,1s}^{(0)}(r;\kappa)G_0(r)/r$ (left y axis) for the $n = 1$ level in hydrogen as well as the screening function (logarithmic right y axis) as function of radius.

for $U_{1s,1s}^{(0)}(r;\kappa)$. This difference is due to the screening cloud associated with the perturber in the screened interaction. Far away the radiator does not interact with the perturber through the monopole term. As an unscreened perturber approaches within the extent of the radiator, the bound electron screening of the nucleus decreases, and the interaction increases diverging at the origin. On the other hand, as a screened perturber approaches, the screening cloud penetrates the radiator before the perturber. Since the cloud has opposite charge to the perturber, it yields a negative contribution as shown in Fig. 2. As the screened perturber gets closer to the nucleus, the bound electron and screening cloud shield less effectively and the interaction approaches the unscreened result. This description applies to neutral and charged radiators since the perturbers are interacting only with the radiator internal states. There is, of course, the V_{net} interaction in either Eq. (6) or Eq. (25) describing the center-of-mass motion, which does not affect the arguments.

V. NUMERICAL METHODS

A variant of computer simulations (CS) described in Ref. [27] is used. Briefly, Eq. (3) is numerically solved by introducing the time-development operator $\mathcal{U}(t)$ in the interaction representation,

$$i\hbar \frac{d\mathcal{U}(t)}{dt} = \hat{V}_I(t)\mathcal{U}(t) \tag{46}$$

with

$$\hat{V}_I(t) = e^{iH_0t/\hbar}V_I(t)e^{-iH_0t/\hbar}. \tag{47}$$

The time evolution of the dipole operator is then given by

$$\vec{d}(t) = \mathcal{U}^\dagger(t)e^{iH_0t/\hbar}\vec{d}e^{-iH_0t/\hbar}\mathcal{U}(t) \tag{48}$$

with Fourier transform

$$\vec{d}(\omega) = \int_0^\infty dt\, e^{i\omega t}\vec{d}(t). \tag{49}$$

Assuming the radiator density matrix is diagonal, which is customary in line shape broadening calculations [5], together

with the Wiener-Khinchin theorem, Eq. (2) can be written as

$$C(t) = \sum_{if} \rho_i \int_0^\infty d\omega\, e^{-i\omega t} \langle |\vec{d}_{fi}(\omega)|^2 \rangle. \tag{50}$$

Finally, Eq. (1) becomes

$$I(\omega) \propto \sum_{if} \rho_i \langle |\vec{d}_{fi}(\omega)|^2 \rangle, \tag{51}$$

where the sums are over initial and final states i and f, respectively, and the plasma average denoted by the angle brackets is accomplished by averaging over CS runs.

A. TMD simulations

The motion of the plasma quasiparticles (both plasma electrons and ions) is described by the screened monopole interaction in Eq. (25) using a velocity Verlet algorithm [31]. The simulation follows the reduced-mass model [18] with a fixed, static radiator at the center of a spherical box of radius several times the electron Debye length to ensure convergence [32]. Whenever a perturber exits the simulation volume, it is reinjected at a random point on the sphere surface with a velocity randomly chosen according to the 2D Gaussian distribution in the tangential plane and Rayleigh distribution in the radial direction. Therefore, the available phase-space is well represented in spite the relatively small number of perturbers. If an electron becomes "bound" (negative kinetic plus potential energy), then it is replaced according to the reinjection procedure above.

Each ion species σ is assigned a different screening length. For a weakly coupled plasma, the inverse screening length κ_σ includes screening by all other charged particles with the same or lesser mass,

$$\kappa_\sigma^2 = \sum_{\sigma'(m_{\sigma'} \leqslant m_\sigma)} \frac{4\pi n_{\sigma'} Z_{\sigma'}^2}{T}, \tag{52}$$

with m_σ and n_σ the mass and number density of species σ in the plasma and T the plasma temperature in hartree energy units. When the plasma coupling is significant (as in the cases considered below) the screening is chosen to reproduce the electric microfield distribution obtained from a fully interacting N-body CS or from the APEX model [33]. For electrons, the Debye screening length is always assumed,

$$\kappa_e^2 = \frac{4\pi n_e}{T}, \tag{53}$$

and dynamic screening is neglected, which is known to be negligible except for a minor effect at detuning energies near the plasma frequency [34,35].

The TMD simulations are verified to be thermodynamically sound. For example, the simulated ion and electron radial distributions functions about the radiator are compared against exact analytical result

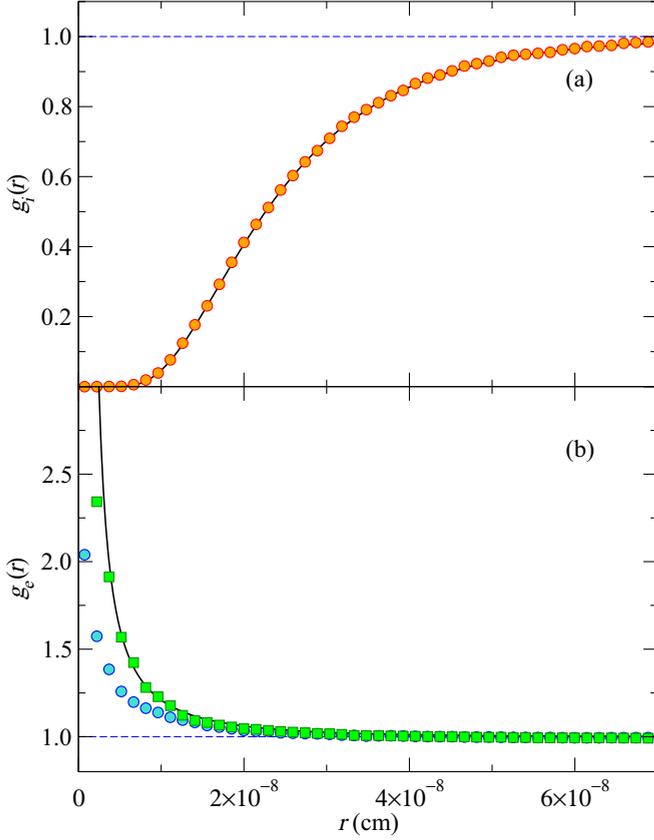$$g_\sigma(r) = \exp\left\{ -\frac{Z_{\text{net}}Z_\sigma}{T} \frac{e^{-\kappa_\sigma r}}{r} \right\} \tag{54}$$

FIG. 3. Examples of radial distribution functions around the radiator ($Z_{net} = 17$). Upper panel: 100 ions, $Z_i = 17$, $n_i = 5.9 \times 10^{22}\,\mathrm{cm}^{-3}$, $T_i = 800\,\mathrm{eV}$, $\kappa_i = 5.3 \times 10^7\,\mathrm{cm}^{-1}$. Lower panel: 1700 electrons, $n_e = 10^{24}\,\mathrm{cm}^{-3}$, $T_e = 800\,\mathrm{eV}$, $\kappa_e = 4.8 \times 10^7\,\mathrm{cm}^{-1}$. The solid lines are analytical results of Eq. (54). Circles are results of TMD, box symbols represent results of simulations with the "bound" electrons allowed.

(recall that Z_σ includes the sign of the perturber charge), which for a finite volume V is rescaled by

$$g'_\sigma(r) = g_\sigma(r) \frac{V}{\int_V dV\, g_\sigma(r)}. \tag{55}$$

The comparisons in Fig. 3 show good agreement. It is emphasized that in the electron case, the results in Fig. 3 retain the "bound" electrons. That is, the analytic expression in Eq. (54) accounts for all possible states of the electrons including resonant and bound orbits. Results excluding the "bound" electrons from the simulations, used in the line shape calculations, are also plotted in Fig. 3 and not surprisingly deviate from Eq. (54) at short distances. Interesting treatments of bound electrons as well as electron recombination and ionization processes using classical MD simulations have been attempted [36–38] but are beyond the scope of the present work.

The Debye potentials are also used to calculate $\hat{V}_I(t)$ in Eq. (46). There are several possible approaches to store time sequences and solve the Heisenberg equation for the radiator dipole. The most general saves the position of all perturbers at every time step demanding substantial storage and I/O resources. Alternatively, a more efficient method separates
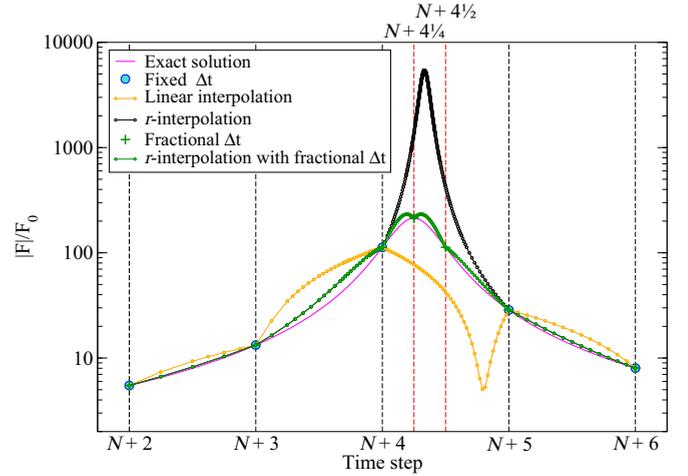

FIG. 4. Magnitude of the dipole electric field (in units of the Holtsmark field F_0) as a function of time during a strong electron collision event using different interpolation approaches. The time scale is in units of the base TMD time step. The small circles indicate time steps of the adaptive ODE solver of Eq. (46), becoming denser for a stronger perturbation.

perturbers into "exact" and "multipole" groups. The scheme only stores the position of "exact" perturbers within a sphere of radius R_{exact} dictated by the requirement of accurate radial integrals (e.g., see Fig. 1 for the Coulomb potential). The number of "exact" perturbers (mostly electrons) is therefore time dependent and in the numerical examples below varies from a few to several tens still constituting a small fraction of the total perturber number. The remaining "multipole" perturbers outside the sphere are treated in the multipole expansion approximation, and the electric field and field gradients are stored as in the usual simulations. In the case where the radiator effective size is much smaller than the plasma screening length (applies to cases considered here), the radiator-perturber interaction reduces to

$$V_I = \vec{r}_a \cdot \vec{F} + \frac{1}{6} \sum_{ij} \frac{dF_i}{dx_j} Q_{ij} + \frac{r_a^2}{6} \vec{\nabla} \cdot \vec{F} \tag{56}$$

with $\vec{F}$ the electric field produced by the "multipole" perturbers at the radiator nucleus, x_i the ith Cartesian component of $\vec{r}_a$, and Q_{ij} the traceless quadrupole radiator moment. The last term has long been a subject of debate but is present in a consistent expansion [11].

B. Time intervals

Sufficiently small time intervals are crucial to track accurately strong radiator-electron collisions in the simulation histories and the differential equation. Although an adaptive time step has long been used for solving the differential equation in the CS simulations [27], interpolation is still necessary to obtain $V_I(t)$ between the fixed time step provided by the CS. The problem becomes acute for close collisions when the electron kinetic energy greatly exceeds the typical thermal energy. Although such collisions are rare, they are important for line broadening and the usual fixed time step proportional
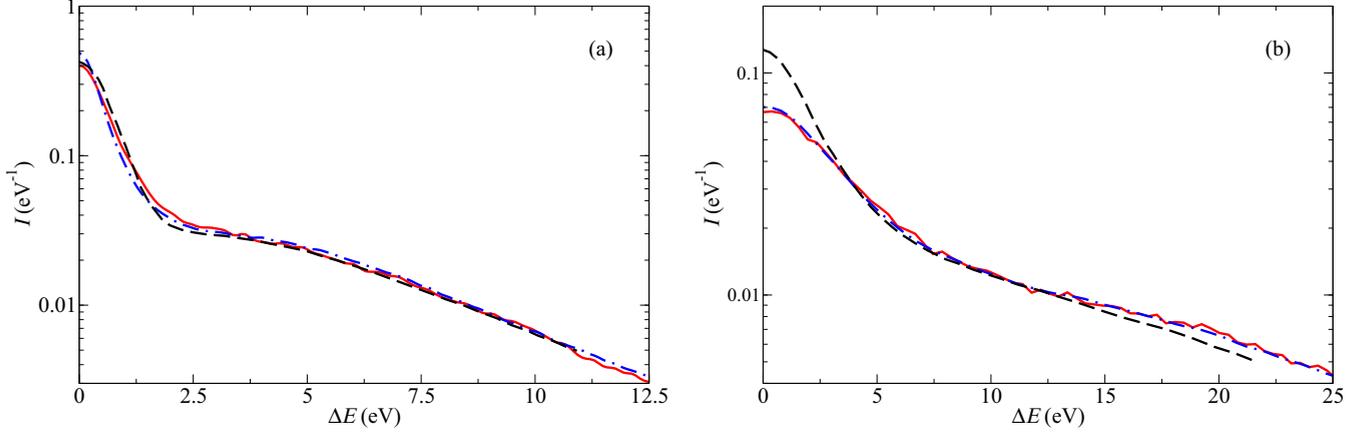
FIG. 5. Shapes of Ar XVIII Ly-α calculated in the dipole approximation assuming $n_e = 10^{24}$ cm^{-3}, $T = 800$ eV (a) and $n_e = 10^{25}$ cm^{-3}, $T = 800$ eV (b). Results of the present work (red solid lines) are compared to those of Ref. [9] (black dashed lines). Also shown are CS results without ion dynamics (blue dot-dashed lines).

to $n_e^{-\frac{1}{3}} \sqrt{m_e/T_e}$ is highly inefficient or inaccurate depending on the proportionality constant. Instead, an adaptive time step is adopted to represent the time histories from the CS.

The criterion requires that the position vector of any perturber not rotate by more than $\pi/2$ radians during a time step as predicted by the Verlet algorithm. If the criterion is not satisfied, the time step is halved until met. An interpolation is performed for values at times between the variable time steps. For "exact" perturbers the position vectors are interpolated. For "multipole" perturbers the quantity $\vec{f} = \vec{F}/F^{3/2}$ is interpolated. That is, for $t_N \leqslant t \leqslant t_{N+1}$

$$\vec{f}(t) = \vec{f}(t_N) + \frac{t - t_N}{t_{N+1} - t_N}[\vec{f}(t_{N+1}) - \vec{f}(t_N)] \qquad (57)$$

followed by $\vec{F} = \vec{f}/f^3$. If the field magnitude is much larger than the typical Holtsmark value, the nearest-neighbor approximation with $\vec{f} \propto \vec{r}$ is valid and, as shown below, provides a better estimate of the field.

The procedure is demonstrated in Fig. 4 with a strong collision event. In the figure, the minimal approach distance (and maximum electric field) occurs between the $N + 4$ and $N + 5$ time step with the electron nearly backscattering. The danger

of using large time intervals is clear, potentially producing orders of magnitude error. On the other hand, adding only two additional time steps the electron trajectory around the perihelion splits into arcs of less than $\pi/2$ radians and suffices to generate good interpolation results.

VI. NUMERICAL RESULTS

Line shape function calculations using the TMD simulations were performed for the lowest members of the Lyman series of hydrogenic Ar at the plasma conditions considered by Woltz and Hooper [9] (hereafter WH), namely, $n_e = 10^{24}$ cm^{-3} and 10^{25} cm^{-3}, $T = 800$ eV, and ion perturbers with $Z_i = 17$. For the sake of comparisons, some simplifying assumptions in WH were adopted: the nonquenching approximation and neglected spin-orbit coupling. For these calculations, the effective screening parameter for the ions was chosen to achieve the best match with the peak of the APEX distribution.

Line shapes from CS for Ly-α, Ly-β, and Ly-γ are offered in Figs. 5–7, respectively, in the "standard" dipole radiator-perturber interaction approximation, which keeps only the first term in Eq. (56) for all perturbers. These are compared
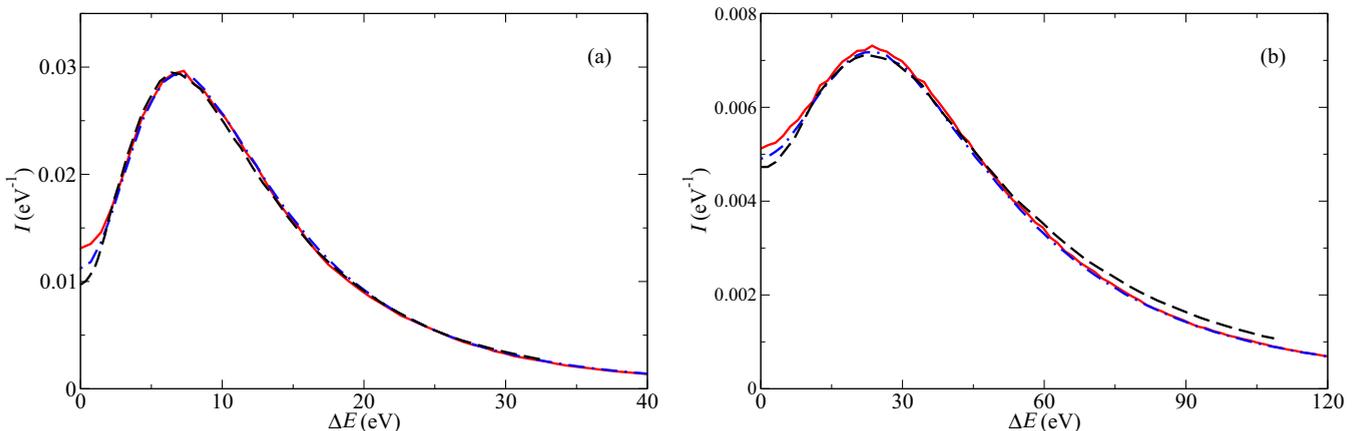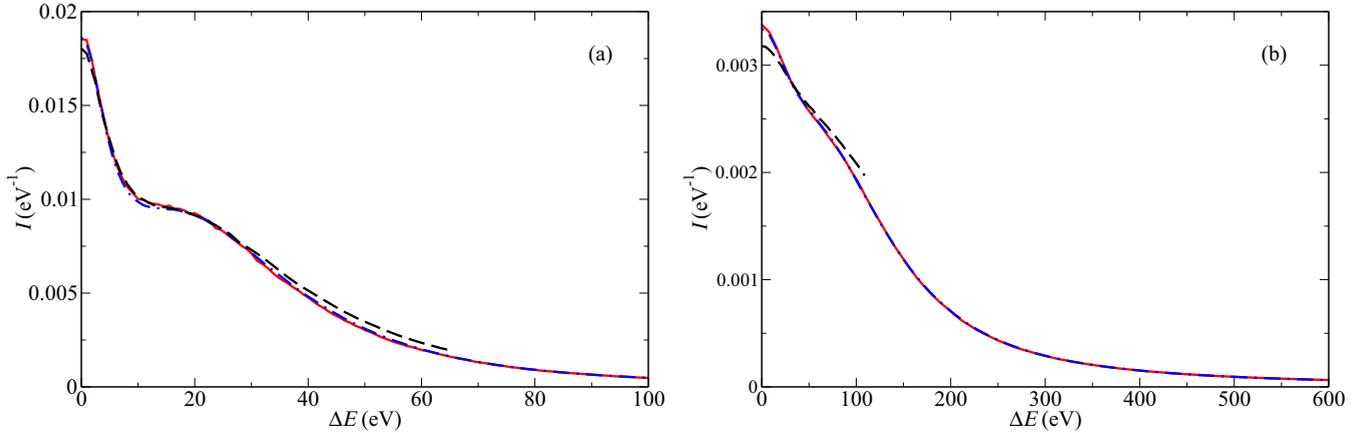

FIG. 6. Same as Fig. 5, but for Ar XVIII Ly-β.

FIG. 7. Same as Fig. 5, but for Ar XVIII Ly-γ.

with the corresponding electron second-order collision theory and quasistatic ion results from WH. The agreement is reasonable at the lower density but worsens at the larger density, particularly about the central part of Ly-α dominated by electrons. To eliminate contribution of ion dynamics, CS calculations were repeated with stationary ions, resulting in minor changes only. Thus, a cause of this discrepancy remains unknown.

For purpose of analysis, it is possible to perform calculations retaining only a subset of the terms in the expansion of the full interaction and results for Ly-α are given in Fig. 8. It follows from the figure that the "standard" dipole approximation overestimates the broadening compared to the full interaction. This is due to a partial cancellation of effects in the latter calculation: (1) reduction of the interaction at small radii and (2) additional broadening from the monopole and quadrupole terms. Similar conclusions were drawn by WH for the lower density case, except they reported a minor increase in line width for the full Coulomb calculation. The nondipole terms are also responsible for a line shift, explicitly neglected by WH. The major contribution is a red shift by the monopole term of penetrating electrons screening the bound electron from the nuclear charge [17] often called the plasma polarization shift (PPS). The PPS is partly offset by

the quadrupole contributions, which do not lead to an overall line shift [39], but rather a line asymmetry due to the central and side components shifting in opposite directions. For these and consequent calculations, R_{exact} (the radius within which electron penetration is treated exactly) is set to be 10^{-8} cm, which is further discussed below.

The Ar XVIII Ly-β line results presented in Fig. 9 are unsurprisingly dominated by the ion microfield displaying the characteristic double peak shape. Consequently, the effects of electron-penetrating collisions are less pronounced. Nevertheless, the same qualitative conclusions can be drawn; the standard dipole approximation overestimates the broadening.

These effects are amplified for higher line series members but without changing the qualitative picture as shown in Fig. 10 for the Ly-γ line. One notable difference is the pronounced asymmetry at the higher density due to the differential shifts from the $\ell = 0$ and $\ell = 2$ terms. The effects discussed above are visible in the far line wings and cannot be solely described by the ion electric microfield distribution. Although less pronounced in the Ly-α and Ly-β lines, the differences can be seen in the logarithmic scale used in Fig. 11. First, the standard dipole approximation substantially overestimates the wings. Second, an accurate description of the far wing requires both the $\ell = 0$ and $\ell = 1$ terms in the
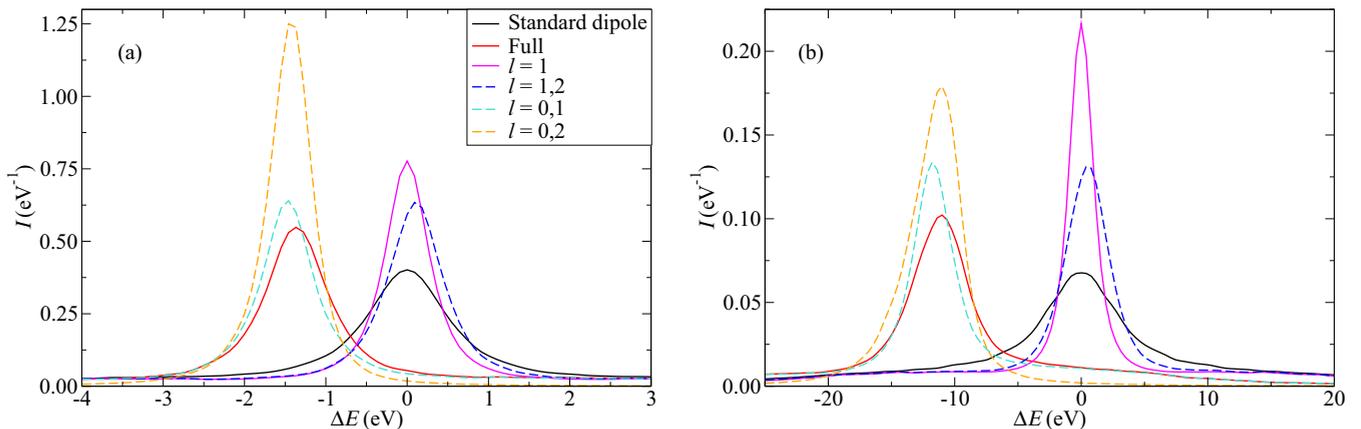

FIG. 8. Shapes of Ar XVIII Ly-α calculated in various schemes for $n_e = 10^{24}$ cm^{-3}, $T = 800$ eV (a) and $n_e = 10^{25}$ cm^{-3}, $T = 800$ eV (b) assumed. Multipole terms retained in Hamiltonian are indicated in the legend. For comparison, shown also are results of the standard dipole approximation (these are the line shapes shown by the solid lines in Fig. 5).
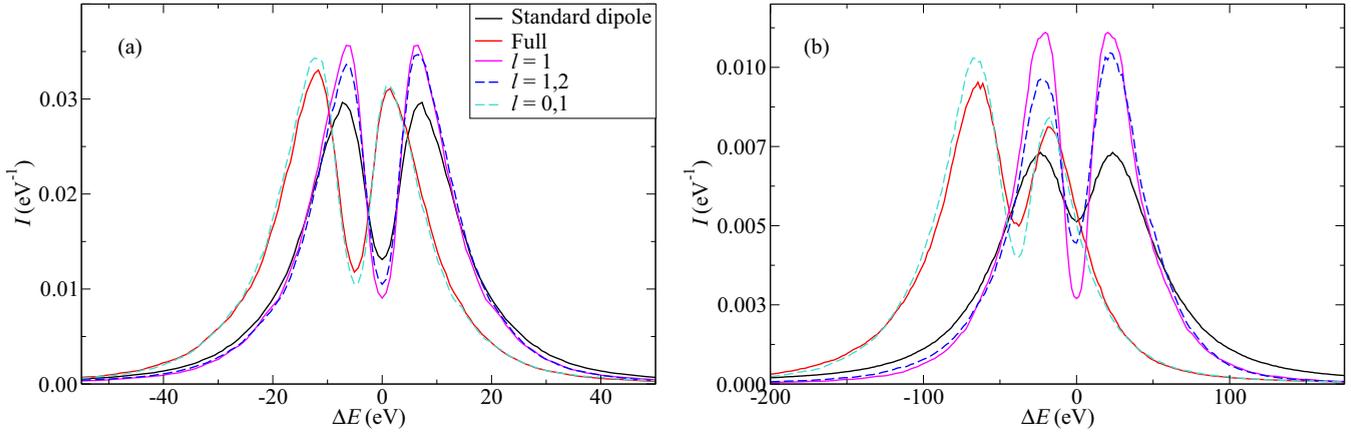
FIG. 9. Same as Fig. 8, but for Ar XVIII Ly-β.

expansion of the full interaction with negligible contributions from the higher poles.

The dependence of the width and shift for the Ly-α line on R_{exact} is shown in Fig. 12. The line width diverges since the quadrupole term goes to infinity for vanishing R_{exact}. This divergence is absent in the $\ell = 2$ term in the expansion of the full interaction. Since most of the shift is due to the PPS, which vanishes without penetrating collisions, the shift requires larger R_{exact} than the width before it converges.

The choice of $R_{\mathrm{exact}} = 10^{-8}$ cm is justified for the Ly-β line in Fig. 13, which shows the line shape converged. Since only the $\ell \leqslant 2$ terms are considered for the "multipole" electrons outside R_{exact}, the convergence in Fig. 13 also demonstrates that higher multipoles are negligible at large radii. Note that calculations neglecting the $\ell > 2$ terms for "exact" electrons inside R_{exact} resulted in nearly indistinguishable results. Thus, keeping only the $\ell \leqslant 2$ terms, which significantly reduces the computational complexity, suffices to produce accurate line shapes.

VII. CONCLUSION

Past calculations of spectral line broadening by plasmas using molecular dynamics have relied on the multipole expansion of the radiator-plasma interaction often only keeping the dipole term. The present work shows how to extend the com-

puter simulations to account for the full Coulomb or screened Coulomb radiator-plasma interactions for hydrogenic systems. The full interaction treatment removes inherent strong collision divergences in the multipole expansion approximation previously avoided with *ad hoc* cutoffs [7]. Furthermore, the full interaction includes the plasma polarization shift produced by perturbers penetrating the wave function of the radiating bound electrons.

A scheme was developed to avoid the extensive I/O requirements in a brute force approach to describe the time-dependent positions of all plasma particles. Instead, a relatively few perturbers near the radiating atomic system need be described in detail while the remaining vast majority are accurately treated by the usual multipole approach only requiring the electric field and field inhomogeneities at the radiator nucleus.

The computer simulation with noninteracting plasma quasiparticles and screened Coulomb radiator-plasma interactions was applied to the hydrogenic Ar Ly-α, Ly-β, and Ly-γ spectral lines in a dense argon plasma at free electron densities of 10^{24} and 10^{25} cm^{-3} and temperature of 800 eV . The results were compared to earlier calculations using full Coulomb radiator-electron interactions in second-order theory and the standard dipole interaction for quasistatic ions [9]. The results are in reasonable agreement at the lower density but
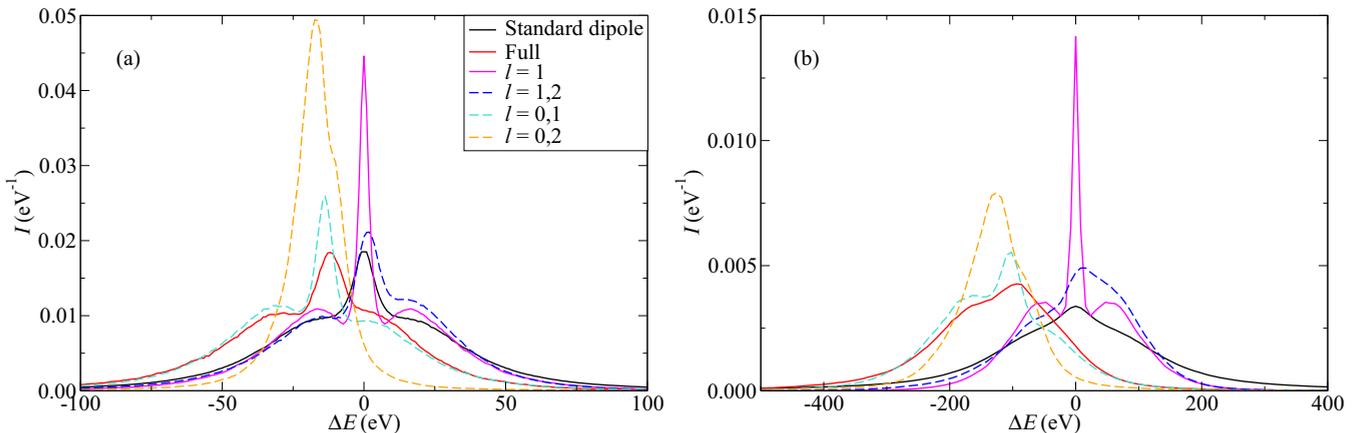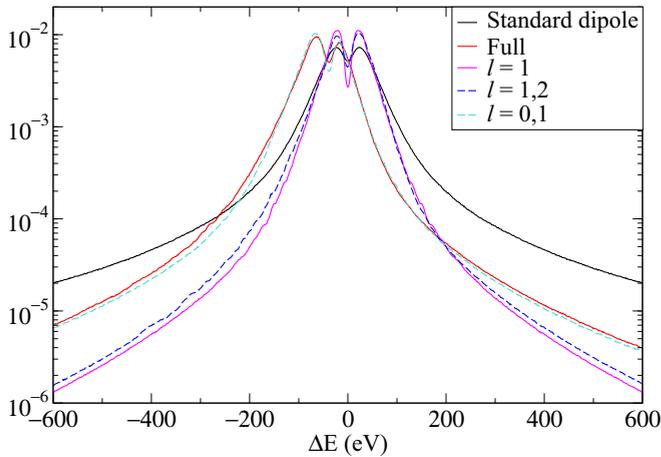

FIG. 10. Same as Fig. 8, but for Ar XVIII Ly-γ.

FIG. 11. Data from Fig. 9(b) presented in the semilogarithmic scale.

significantly differ at the higher one in the case of Ly-α. It was found, in qualitative agreement with the previous work, that the "standard" dipole approximation overestimates the broadening compared to the dipole term in the exact interaction but contribution of the $\ell \neq 1$ poles, mostly monopole and quadrupole, roughly compensates for the difference. Furthermore, it was shown that the far line wings are not accurately described by the standard dipole approximation. Instead, the wings depend on both the $\ell = 0$ and $\ell = 1$ terms in the partial wave expansion of the full radiator-perturber interaction. The monopole term also contributes to a significant shift and a line shape asymmetry. To a lesser extent, the quadrupole interaction is another source of asymmetry, resulting in an apparent minor shift of lines with a central component (Ly-α, Ly-γ) in the direction opposite to that of the monopole PPS.

With the line shape, including the shift, obtained with minimal approximating assumptions, the present approach is important for diagnostics of various plasmas, including cases where a precise relation between the width and shift is crucial
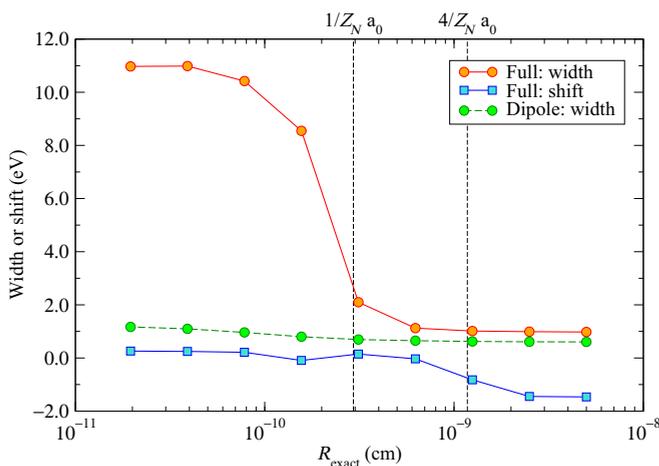

FIG. 12. The width (FWHM) and shift of Ar XVIII Ly-α as a function of R_{exact} assuming $n_e = 10^{24}\,\text{cm}^{-3}$ and $T = 800\,\text{eV}$. Typical extension sizes of the $n = 1$ and $n = 2$ electron-shell clouds are indicated, in units of the Z_N-scaled ($Z_N = 18$) Bohr radius.
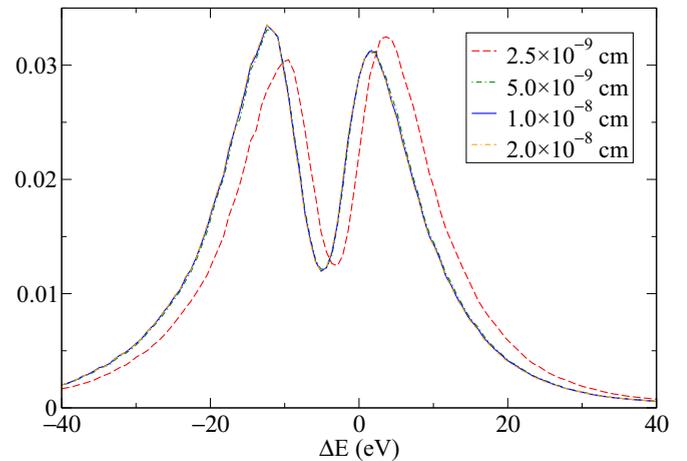

FIG. 13. Ar XVIII Ly-β shapes calculated for various values of R_{exact} (indicated in the legend) assuming $n_e = 10^{24}\,\text{cm}^{-3}$ and $T = 800\,\text{eV}$.

[40] or presents a challenge [41]. A few possible directions for extending the approach exist. One is using full MD (FMD) accounting for the Coulomb interactions between all particles, eliminating the Debye quasiparticle approximation of TMD. The significantly increased computational costs imposed by FMD would be partly offset by the simpler calculation of V_I (cf. expressions in Appendixes B and C). Note that the optimization techniques used in this study (separation of the perturbers into "exact" and "multipole" groups, and adaptive time steps for storing field and perturber coordinate histories) are equally applicable to FMD. In any variant of MD, the motion of a perturber penetrating the bound electron cloud of the radiator is governed by the monopole interaction with an effective $Z^*(r)$, in general $Z_N < Z^* < Z_N + 1$. For $Z_N \gg 1$, as in the present work, this correction is largely unimportant. However, for neutral or weakly ionized radiators this effect should be investigated. Application to nonhydrogenic, multielectron radiators will require numerical evaluation of matrix elements on a grid of r with the radial functions provided by an atomic structure package (e.g., [21,22]) and using interpolation. Even for hydrogen-like radiators, more complex calculations may be required for accurate line shape modeling. For example, the spin-orbit coupling, neglected in the present calculations, is substantial for the Ar XVIII Ly-α line, exceeding the width of its central Stark component at the lowest density considered here. Furthermore, inelastic ("quenching") collisions between states with different n's also contribute to the line width and shift. A comparison made in Ref. [9] with earlier full-Coulomb calculations [42] indicated a modest effect (10%–20%) of the quenching collisions on the Ly-α and Ly-β broadening at $10^{24}\,\text{cm}^{-3}$. On the other hand, towards higher density the Ly-γ shape will likely be strongly affected, entirely disappearing at $10^{25}\,\text{cm}^{-3}$ due to the ionization potential depression [43].

APPENDIX A: REDUCED MATRIX ELEMENTS FOR HYDROGENIC RADIATORS

For hydrogenic systems the reduced matrix elements are written in terms of $3n$-j symbols [21]. For arbitrary radial function $f(r_a)$

$$\sqrt{\frac{4\pi}{2\ell+1}} \langle \alpha \| f(r_a) Y_{\ell m}(\hat{r}_a) \| \beta \rangle$$
$$= A_{\alpha\beta}^{(\ell)} \int_0^\infty dr_a P_\alpha(r_a) f(r_a) P_\beta(r_a), \qquad (A1)$$

where $P_\alpha(r)$ is the hydrogenic reduced radial wave function for the isolated radiator state $|\alpha\rangle$.

For states including fine structure, that is, $|\alpha\rangle = |n_\alpha \ell_\alpha s_\alpha j_\alpha m_\alpha\rangle$ with n_α, ℓ_α, and s_α respectively the principal, orbital, and spin quantum numbers, plus j_α and m_α the total angular momentum and magnetic quantum numbers, the angular factors are given by

$$A_{\alpha\beta}^{(\ell)} = \delta_{s_\alpha s_\beta} (-1)^{j_\beta+\frac{1}{2}}$$
$$\times \sqrt{(2j_\alpha+1)(2j_\beta+1)(2\ell_\alpha+1)(2\ell_\beta+1)}$$
$$\times \begin{Bmatrix} \ell_\alpha & s_\alpha & j_\alpha \\ j_\beta & \ell & \ell_\beta \end{Bmatrix} \begin{pmatrix} \ell_\alpha & \ell & \ell_\beta \\ 0 & 0 & 0 \end{pmatrix} \qquad (A2)$$

If neglecting spin, then the state is described by $|\alpha\rangle = |n_\alpha \ell_\alpha m_\alpha\rangle$ and

$$A_{\alpha\beta}^{(\ell)} = (-1)^{\ell_\alpha} \sqrt{(2\ell_\alpha+1)(2\ell_\beta+1)} \begin{pmatrix} \ell_\alpha & \ell & \ell_\beta \\ 0 & 0 & 0 \end{pmatrix} \quad (A3)$$

It follows from the 3-j symbol that for $\ell = 0$ the reduced matrix elements are diagonal in orbital angular momentum quantum numbers.

APPENDIX B: ATOMIC INTEGRALS FOR COULOMB INTERACTION

The radial contribution to the atomic matrix elements for the full Coulomb radiator-perturber interaction in Eq. (17) is given by

$$U_{\alpha\beta}^{(\ell)}(r) = \int_0^\infty dr_a P_\alpha(r_a) \left(\frac{\delta_{\ell 0}}{r} - \frac{r_<^\ell}{r_>^{\ell+1}} \right) P_\beta(r_a), \qquad (B1)$$

where $P_\alpha(r_a)$ is the reduced radial wave function for radiator internal state $|\alpha\rangle$. These integrals yield analytical results for hydrogenic wave functions [23] and scale as [21]

$$U_{\alpha\beta}^{(\ell)}(r; Z_N) = Z_N U_{\alpha\beta}^{(\ell)}(r \to Z_N r; Z_N = 1) \qquad (B2)$$

with Z_N the radiator nuclear charge. In addition, for $\ell \geqslant 1$ the radial matrix elements can be expressed in the form

$$U_{\alpha\beta}^{(\ell)}(r; Z_N = 1) = -\frac{R_{\alpha\beta}^{(\ell)}}{r^{\ell+1}} \left[1 - e^{-(n_a+n_b)r/(n_a n_b)} p_{\alpha\beta}^{(\ell)}(r) \right] \tag{B3}$$

with $p(r)$ a polynomial in r. As mentioned in Sec. III B, for perturbers sufficiently distant from the radiator a simplified treatment is possible by neglecting the second term in Eq. (B3).

Expressions are provided for the hydrogen Ly-α line. These were generated using an algebraic language [44], which also generates FORTRAN or C forms minimizing errors in coding. The $r \to 0$ limits are useful for numerical calculations. There are respectively 10 and 20 terms for the Ly-β and Ly-γ lines, and the expressions are lengthy and consequently not included but available on request.

1. Principal quantum number $n = 1$

The angular factors constrain the calculations to one radial integral,

$$U_{1s,1s}^{(0)}(r) = \frac{e^{-2r}}{r}(1+r)$$
$$= \frac{1}{r} - 1 + \frac{2r^2}{3} + \frac{2r^3}{3} + O(r^4). \qquad (B4)$$

2. Principal quantum number $n = 2$

The angular factors constrain the calculations to only four radial integrals,

$$U_{2s,2s}^{(0)}(r) = \frac{e^{-r}}{8r}(8+6r+2r^2+r^3)$$
$$= \frac{1}{r} - \frac{1}{4} + \frac{r^2}{12} - \frac{r^3}{12} + O(r^4), \qquad (B5)$$

$$U_{2p,2p}^{(0)}(r) = \frac{e^{-r}}{24r}(24+18r+6r^2+r^3)$$
$$= \frac{1}{r} - \frac{1}{4} + \frac{r^4}{480} - \frac{r^5}{720} + O(r^6), \qquad (B6)$$

$$U_{2s,2p}^{(1)}(r) = \frac{3\sqrt{3}}{r^2} \left(1 - e^{-r} \sum_{j=0}^4 \frac{r^j}{j!} \right)$$
$$= \frac{\sqrt{3}}{40} r^3 \left(1 - \frac{5r}{6} + \frac{5r^2}{14} \right) + O(r^6), \qquad (B7)$$

and

$$U_{2p,2p}^{(2)}(r) = -\frac{30}{r^3} \left[1 - e^{-r} \left(\sum_{j=0}^4 \frac{r^j}{j!} + \frac{r^5}{144} \right) \right]$$
$$= -\frac{r^2}{24} \left(1 - \frac{5r^2}{14} + \frac{5r^3}{24} \right) + O(r^6). \qquad (B8)$$

APPENDIX C: ATOMIC INTEGRALS FOR SCREENED COULOMB INTERACTION

The radial matrix elements for the screened Coulomb potential are defined in Eq. (30) as

$$
U_{\alpha\beta}^{(\ell)}(r;\kappa) = \delta_{\alpha\beta}\delta_{\ell 0}\frac{e^{-\kappa r}}{r} - \frac{2\ell+1}{\sqrt{r}}
$$
$$
\times \int_0^\infty \frac{dr_a}{\sqrt{r_a}}P_\alpha(r_a)I_{\ell+\frac{1}{2}}(\kappa r_<)K_{\ell+\frac{1}{2}}(\kappa r_>)P_\beta(r_a)
$$
(C1)

with $I_\mu(x)$ and $K_\mu(x)$ modified Bessel functions of the first and third kind, respectively [26]. These integrals scale as

$$
U_{\alpha\beta}^{(\ell)}(r;\kappa;Z_N) = Z_N U_{\alpha\beta}^{(\ell)}(Z_N r;Z_N^{-1}\kappa) \tag{C2}
$$

for nuclear charge Z_N. The separation in Eq. (32) has the short-ranged contribution $B_{\alpha\beta}^{(\ell)}(r;\kappa)$ that scales the same as Eq. (C2). The long-range contribution in Eq. (32) scales as

$$
R_{\alpha\beta}^{(\ell)}(\kappa;Z_N)G_\ell(r;\kappa) = Z_N R_{\alpha\beta}^{(\ell)}(Z_N^{-1}\kappa)G_\ell(Z_N r;Z_N^{-1}\kappa) \tag{C3}
$$

and is consistent with Eq. (C2). As for the Coulomb case, only results for the Ly-α line are provided below.

1. Principal quantum number $n = 1$

The angular factors limit the matrix elements to the monopole term,

$$
R_{1s,1s}^{(0)}(\kappa) = \frac{\kappa^2(8-\kappa^2)}{(4-\kappa^2)^2} \tag{C4}
$$

and

$$
B_{1s,1s}^{(0)}(r;\kappa) = 4\frac{e^{-2r}}{r}\frac{4(1+r)-\kappa^2 r}{(4-\kappa^2)^2}, \tag{C5}
$$

conditional on a screening length sufficiently large to make $\kappa < 2$ (recall length units are in Bohr radius) or the integral diverges. This restriction on κ is a result of the separation into short- and long-ranged contributions. That is, Eq. (C1) yields

$$
U_{1s,1s}^{(0)}(r;\kappa) = \frac{1}{(4-\kappa^2)^2 r}
$$
$$
\times \{(\kappa^2-8)\kappa^2 e^{-\kappa r} + 4[1+(4-\kappa^2)r]e^{-2r}\}
$$
$$
= \frac{1}{r} - \left(\kappa + \frac{4}{(2+\kappa)^2}\right) + \frac{\kappa^2 r}{2}
$$
$$
+ \frac{16+16\kappa-\kappa^3(2+\kappa)^2}{6(2+\kappa)^2}r^2 + O(r^3), \tag{C6}
$$

which is valid for all $\kappa \geqslant 0$. Furthermore,

$$
U_{1s,1s}^{(0)}(r;\kappa \to 2) = \frac{e^{-2r}}{r}\left(1 - \frac{r}{4} - \frac{r^2}{2}\right) \tag{C7}
$$

and does not diverge despite the denominator in Eq. (C6).

2. Principal quantum number $n = 2$

There are four terms. The radiator moments are

$$
R_{2s,2s}^{(0)}(\kappa) = \frac{\kappa^2(7-4\kappa^2+4\kappa^4-\kappa^6)}{(1-\kappa^2)^4}, \tag{C8}
$$

$$
R_{2p,2p}^{(0)}(\kappa) = \frac{\kappa^2(5-6\kappa^2+4\kappa^4-\kappa^6)}{(1-\kappa^2)^4}, \tag{C9}
$$

$$
R_{2s,2p}^{(1)}(\kappa) = -\frac{3\sqrt{3}(1+\kappa^2)}{(1-\kappa^2)^4}, \tag{C10}
$$

and

$$
R_{2p,2p}^{(2)}(\kappa) = \frac{30}{(1-\kappa^2)^4}, \tag{C11}
$$

which are conditional on $\kappa < 1$. For the short-ranged contributions one gets

$$
B_{2s,2s}^{(0)}(r;\kappa) = \frac{1}{8(1-\kappa^2)^4}\frac{e^{-r}}{r}\left[(8+6r+2r^2+r^3) + \kappa^2(24+8r-3r^3) + \kappa^4(16-10r-6r^2+3r^3) + \kappa^6 r(4+4r-r^2)\right], \tag{C12}
$$

$$
B_{2p,2p}^{(0)}(r;\kappa) = \frac{1}{24(1-\kappa^2)^4}\frac{e^{-r}}{r}[(24+18r+6r^2+r^3) + 3\kappa^2(8-4r-4r^2-r^3) - 3\kappa^4 r(2-2r-r^2) - \kappa^6 r^3], \tag{C13}
$$

$$
B_{2s,2p}^{(1)}(r;\kappa) = -\frac{\sqrt{3}}{8(1-\kappa^2)^4}\frac{e^{-r}}{r^2}[(24+24r+12r^2+4r^3+r^4) + 3\kappa^2(8+8r-2r^3-r^4) - 3\kappa^4 r^2(4-r^2) + \kappa^6 r^3(2-r)], \tag{C14}
$$

and

$$
B_{2p,2p}^{(2)}(r;\kappa) = \frac{5}{24(1-\kappa^2)^4}\frac{e^{-r}}{r^3}[(144+144r+72r^2+24r^3+6r^4+r^5) - 3\kappa^2 r^2(8+8r+4r^2+r^3) + 3\kappa^4 r^4(2+r) - \kappa^6 r^5], \tag{C15}
$$

also conditional on $\kappa < 1$.

Explicit expressions of $U_{\alpha\beta}^{(\ell)}(r;\kappa)$ for $n = 2$ are not provided since they are available by combining results above using Eq. (32). Instead, results for $U_{\alpha\beta}^{(\ell)}(r \to 0;\kappa)$ are given, which are convenient for numerical calculations:

$$U_{2s,2s}^{(0)}(r;\kappa) = \frac{1}{r} - \left[\kappa + \frac{1 + 2\kappa^2}{4(1 + \kappa)^4}\right] + \frac{\kappa^2 r}{2} + \left\{\frac{1}{2} - \left[\kappa + \frac{1 + 2\kappa^2}{4(1 + \kappa)^4}\right]\kappa^2\right\}\frac{r^2}{6} + O(r^3), \tag{C16}$$

$$U_{2p,2p}^{(0)}(r;\kappa) = \frac{1}{r} - \left[\kappa + \frac{1}{4(1 + \kappa)^4}\right] + \frac{\kappa^2 r}{2} - \left[\kappa + \frac{1}{4(1 + \kappa)^4}\right]\frac{\kappa^2 r^2}{6} + O(r^3), \tag{C17}$$

$$U_{2s,2p}^{(1)}(r;\kappa) = -\frac{\kappa^2 r\sqrt{3}}{4(1 + \kappa)^4}\left[1 - \frac{1 + 4\kappa + 6\kappa^2 + 4\kappa^3}{10\kappa^2}r^2 + \frac{(1 + \kappa)^4}{12\kappa^2}r^3 + O(r^4)\right], \tag{C18}$$

and

$$U_{2p,2p}^{(2)}(r;\kappa) = -\frac{r^2}{24(1 + \kappa)^4}\left[(1 + 4\kappa + 5\kappa^2) - \frac{5 + 20\kappa + 29\kappa^2 + 16\kappa^3}{14}r^2 + \frac{5(1 + \kappa)^4}{24}r^3 + O(r^4)\right]. \tag{C19}$$

3. Expressions for $G_\ell(r;\kappa)$

Using known properties of the Bessel function [45], write

$$G_\ell(r;\kappa) = -\frac{(-r)^\ell}{(2\ell - 1)!!}\left(\frac{1}{r}\frac{\partial}{\partial r}\right)^\ell \frac{e^{-\kappa r}}{r}, \tag{C20}$$

which yields

$$G_0(r;\kappa) = -\frac{e^{-\kappa r}}{r}, \tag{C21}$$

$$G_1(r;\kappa) = -\frac{e^{-\kappa r}}{r^2}(1 + \kappa r), \tag{C22}$$

$$G_2(r;\kappa) = -\frac{e^{-\kappa r}}{r^3}\left(1 + \kappa r + \frac{\kappa^2 r^2}{3}\right), \tag{C23}$$

$$G_3(r;\kappa) = -\frac{e^{-\kappa r}}{r^4}\left(1 + \kappa r + \frac{2\kappa^2 r^2}{5} + \frac{2\kappa^3 r^3}{15}\right), \tag{C24}$$

and

$$G_4(r;\kappa) = -\frac{e^{-\kappa r}}{r^5}\left(1 + \kappa r + \frac{3\kappa^2 r^2}{7} + \frac{2\kappa^3 r^3}{21} + \frac{\kappa^4 r^4}{105}\right), \tag{C25}$$

required in the present work.

APPENDIX D: PENETRATING COLLISIONS

The contribution from penetrating collisions in the radial matrix elements are given in Eq. (37),

$$B_{\alpha\beta}^{(\ell)}(r;\kappa) = (2\ell + 1)\int_r^\infty \frac{dr_a}{\sqrt{r_a r}}P_\alpha(r_a)P_\beta(r_a)$$
$$\times \left[I_{\ell+\frac{1}{2}}(\kappa r_a)K_{\ell+\frac{1}{2}}(\kappa r) - I_{\ell+\frac{1}{2}}(\kappa r)K_{\ell+\frac{1}{2}}(\kappa r_a)\right]. \tag{D1}$$

Using the known expression for the hydrogenic wave functions [21], write

$$P_\alpha(r_a) \propto e^{-r_a/n_\alpha}f_\alpha(r_a) \tag{D2}$$

with $f_\alpha(x)$ a polynomial in x. The modified Bessel function of the third kind can be written as

$$\sqrt{\frac{2}{\pi z}}K_{\ell+\frac{1}{2}}(z) = \frac{e^{-z}}{z^\ell}\chi_\ell(z) \tag{D3}$$

with $\chi_\ell(z)$ a polynomial in z. The modified Bessel function of the first kind has the asymptotic expansion

$$\sqrt{\frac{2}{\pi z}}I_{\ell+\frac{1}{2}}(z) = \frac{e^z}{z}\xi_\ell(z) = \frac{e^z}{z}\sum_{j=0}^\infty \frac{b_j^{(\ell)}}{z^j} \tag{D4}$$

defining $\xi_\ell(z)$ with $b_j^{(\ell)}$ constant coefficients.

Collecting results, the first term in Eq. (D1) is proportional to

$$\frac{\chi_\ell(\kappa r)}{r^\ell}\int_r^\infty dr_a \exp\left(-\frac{n_\alpha + n_\beta}{n_\alpha n_\beta}r_a\right)$$
$$\times f_\alpha(r_a)f_\beta(r_a)e^{-\kappa(r-r_a)}\frac{\xi_\ell(\kappa r_a)}{r_a}$$
$$= \exp\left(-\frac{n_\alpha + n_\beta}{n_\alpha n_\beta}r\right)\frac{\chi_\ell(\kappa r)}{r^\ell}$$
$$\times \int_0^\infty dx \exp\left[-\left(\frac{n_\alpha + n_\beta}{n_\alpha n_\beta} - \kappa\right)x\right]F_1(x + r). \tag{D5}$$

The second term in Eq. (D1) is proportional to

$$\frac{\xi_\ell(\kappa r)}{r}\int_r^\infty dr_a \exp\left(-\frac{n_\alpha + n_\beta}{n_\alpha n_\beta}r_a\right)$$
$$\times f_\alpha(r_a)f_\beta(r_a)e^{-\kappa(r-r_a)}\frac{\chi_\ell(\kappa r_a)}{r_a^\ell}$$
$$= \exp\left(-\frac{n_\alpha + n_\beta}{n_\alpha n_\beta}r\right)\frac{\xi_\ell(\kappa r)}{r}$$
$$\times \int_0^\infty dx \exp\left[-\left(\frac{n_\alpha + n_\beta}{n_\alpha n_\beta} + \kappa\right)x\right]F_2(x + r), \tag{D6}$$

where

$$\left.\begin{array}{c}F_1(x)\\F_2(x)\end{array}\right\} = f_\alpha(x)f_\beta(x)\left\{\begin{array}{c}\xi_\ell(\kappa x)/x\\\chi_\ell(\kappa x)/x^\ell\end{array}\right.. \tag{D7}$$

Both integrands vanish as $x \to \infty$ with the condition [required only for Eq. (D5)]

$$0 \leqslant \kappa < \frac{n_\alpha + n_\beta}{n_\alpha n_\beta}, \tag{D8}$$

leading to finite integrals. Thus,

$$B_{\alpha\beta}^{(\ell)}(r \to \infty; \kappa) \propto \exp\left(-\frac{n_\alpha + n_\beta}{n_\alpha n_\beta} r\right) \qquad \text{(D9)}$$

and the penetrating collision contributions vanish exponentially with perturber distance.

[1] R. Stamm and D. Voslamber, On the role of ion dynamics in the Stark broadening of hydrogen lines, J. Quant. Spectrosc. Radiat. Transfer **22**, 599 (1979).

[2] B. Talin, E. Dufour, A. Calisti, M. A. Gigosos, M. A. González, T. del Río Gaztelurrutia, and J. W. Dufty, Molecular dynamics simulation for modelling plasma spectroscopy, J. Phys. A: Math. Gen. **36**, 6049 (2003).

[3] E. Stambulchik and Y. Maron, Plasma line broadening and computer simulations: A mini-review, High Energy Density Phys. **6**, 9 (2010).

[4] M. A. Gigosos, Stark broadening models for plasma diagnostics, J. Phys. D: Appl. Phys. **47**, 343001 (2014).

[5] H. R. Griem, *Spectral Line Broadening by Plasmas* (Academic, New York, 1974).

[6] D. B. Boercker and C. A. Iglesias, Static and dynamic shifts of spectral lines, Phys. Rev. A **30**, 2771 (1984).

[7] T. Wujec, W. Olchawa, J. Halenka, and J. Musielok, Experimental and theoretical Stark broadening studies of the hydrogen Paschen beta line, Phys. Rev. E **66**, 066403 (2002).

[8] T. A. Gomez, T. Nagayama, D. P. Kilcrease, M. H. Montgomery, and D. E. Winget, Effect of higher-order multipole moments on the Stark line shape, Phys. Rev. A **94**, 022501 (2016).

[9] L. A. Woltz and C. F. Hooper, Full Coulomb calculation of Stark broadening in laser-produced plasmas, Phys. Rev. A **30**, 468 (1984).

[10] S. Alexiou, Enhancement of line broadening in plasmas by penetrating collisions for hydrogenlike lines, High Energy Density Phys. **23**, 188 (2017).

[11] C. A. Iglesias, Penetrating collisions in hydrogen spectral line broadening by plasmas, High Energy Density Phys. **35**, 100743 (2020).

[12] T. A. Gomez, T. Nagayama, P. B. Cho, M. C. Zammit, C. J. Fontes, D. P. Kilcrease, I. Bray, I. Hubeny, B. H. Dunlap, M. H. Montgomery, and D. E. Winget, All-Order Full-Coulomb Quantum Spectral Line-Shape Calculations, Phys. Rev. Lett. **127**, 235001 (2021).

[13] M.-A. Schaeuble, T. Nagayama, J. E. Bailey, T. A. Gomez, M. H. Montgomery, and D. E. Winget, Hβ and Hγ absorption-line profile inconsistencies in laboratory experiments performed at white dwarf photosphere conditions, Astrophys. J. **885**, 86 (2019).

[14] S. Djurović, M. Ćirišan, A. V. Demura, G. V. Demchenko, D. Nikolić, M. A. Gigosos, and M. Á. González, Measurements of Hβ Stark central asymmetry and its analysis through standard theory and computer simulations, Phys. Rev. E **79**, 046402 (2009).

[15] A. V. Demura, Beyond the linear Stark effect: A retrospective, Atoms **6**, 33 (2018).

[16] T. A. Gomez, T. Nagayama, P. B. Cho, D. P. Kilcrease, C. J. Fontes, and M. C. Zammit, Introduction to spectral line shape theory, J. Phys. B: At. Mol. Opt. Phys. **55**, 034002 (2022).

[17] G. C. Junkel, M. A. Gunderson, C. F. Hooper, and D. A. Haynes, Full Coulomb calculation of Stark broadened spectra from multielectron ions: A focus on the dense plasma line shift, Phys. Rev. E **62**, 5584 (2000).

[18] J. Seidel and R. Stamm, Effects of radiator motion on plasma-broadened hydrogen Lyman-β, J. Quant. Spectrosc. Radiat. Transfer **27**, 499 (1982).

[19] R. Stamm, B. Talin, E. L. Pollock, and C. A. Iglesias, Ion-dynamic effects on the line shapes of hydrogenic emitters in plasmas, Phys. Rev. A **34**, 4144 (1986).

[20] C. A. Iglesias, Reformulation of plasma spectral line broadening with computer simulations, High Energy Density Phys. **33**, 100707 (2019).

[21] R. D. Cowan, *The Theory of Atomic Structure and Spectra* (University of California Press, Berkeley, 1981).

[22] M. F. Gu, The flexible atomic code, Can. J. Phys. **86**, 675 (2008).

[23] B. Zygelman and A. Dalgarno, Impact excitation of the $n = 2$ fine-structure levels in hydrogenlike ions by protons and electrons, Phys. Rev. A **35**, 4085 (1987).

[24] S. Alexiou and A. Poquérusse, Standard line broadening impact theory for hydrogen including penetrating collisions, Phys. Rev. E **72**, 046404 (2005).

[25] S. Pasternack and R. M. Sternheimer, An orthogonality property of hydrogenlike radial functions, J. Math. Phys. **3**, 1280 (1962).

[26] M. Abramowitz and I. A. Stegun, *Handbook of Mathematical Functions with Formulas, Graphs, and Mathematical Tables*, Applied Mathematical Series No. 55 (U.S. Government Printing Office, Washington, DC, 1972).

[27] E. Stambulchik and Y. Maron, A study of ion-dynamics and correlation effects for spectral line broadening in plasma: K-shell lines, J. Quant. Spectrosc. Radiat. Transfer **99**, 730 (2006).

[28] C. Stehlé, D. Gilles, and A. Demura, Asymmetry of Stark profiles, Eur. Phys. J. D **12**, 355 (2000).

[29] J. Halenka and W. Olchawa, Inhomogeneity tensors of ion microfield in Debye plasma at neutral emitter, Eur. Phys. J. D **42**, 425 (2007).

[30] C. A. Iglesias, Multipole interaction in spectral line broadening by plasmas, High Energy Density Phys. **38**, 100921 (2021).

[31] L. Verlet, Computer "experiments" on classical fluids. I. Thermodynamic properties of Lennard-Jones molecules, Phys. Rev. **159**, 98 (1967).

[32] J. Rosato, H. Capes, and R. Stamm, Ideal Coulomb plasma approximation in line shape models: Problematic issues, Atoms **2**, 253 (2014).

[33] C. A. Iglesias, F. J. Rogers, R. Shepherd, A. Bar-Shalom, M. S. Murillo, D. P. Kilcrease, A. Calisti, and R. W. Lee, Fast electric microfield distribution calculations in extreme matter conditions, J. Quant. Spectrosc. Radiat. Transfer **65**, 303 (2000).

[34] T. Hussey, J. W. Dufty, and C. F. Hooper, Kinetic theory of spectral line broadening, Phys. Rev. A **12**, 1084 (1975).

[35] D. B. Boercker, R. W. Lee, and F. J. Rogers, Strong coupling effects on plasma lineshapes and Thomson scattering signals, J. Phys. B: At. Mol. Opt. Phys. **16**, 3279 (1983).

[36] A. Calisti, S. Ferri, and B. Talin, Classical molecular dynamics model for coupled two component plasmas, High Energy Density Phys. **5**, 307 (2009).

[37] A. Calisti and B. Talin, Classical molecular dynamics model for coupled two-component plasmas—Ionization balance and time considerations, Contrib. Plasma Phys. **51**, 524 (2011).

[38] F. R. Graziani, V. S. Batista, L. X. Benedict, J. I. Castor, H. Chen, S. N. Chen, C. A. Fichtl, J. N. Glosli, P. E. Grabowski, A. T. Graf, S. P. Hau-Riege, A. U. Hazi, S. A. Khairallah, L. Krauss, A. B. Langdon, R. A. London, A. Markmann, M. S. Murillo, D. F. Richards, H. A. Scott *et al.*, Large-scale molecular dynamics simulations of dense plasmas: The Cimarron project, High Energy Density Phys. **8**, 105 (2012).

[39] E. Oks, New type of shift of hydrogen and hydrogenlike spectral lines, J. Quant. Spectrosc. Radiat. Transfer **58**, 821 (1997).

[40] B. F. Kraus, L. Gao, K. W. Hill, M. Bitter, P. C. Efthimion, T. A. Gomez, A. Moreau, R. Hollinger, S. Wang, H. Song, J. J. Rocca, and R. C. Mancini, Solid-Density Ion Temperature from Redshifted and Double-Peaked Stark Line Shapes, Phys. Rev. Lett. **127**, 205001 (2021).

[41] C. Stollberg, E. Stambulchik, B. Duan, M. A. Gigosos, D. G. Herrero, C. A. Iglesias, and C. Mossé, Revisiting Stark width and shift of He II Pα, Atoms **6**, 23 (2018).

[42] H. R. Griem, M. Blaha, and P. C. Kepple, Stark-profile calculations for Lyman-series lines of one-electron ions in dense plasmas, Phys. Rev. A **19**, 2421 (1979).

[43] B. J. B. Crowley, Continuum lowering—A new perspective, High Energy Density Phys. **13**, 84 (2014).

[44] Wolfram Research, Inc., Mathematica, version 11.3 (2018).

[45] G. B. Arfken, H. J. Weber, and F. E. Harris, *Mathematical Methods for Physicists*, 7th ed. (Academic, Boston, 2013).